Journal of Sound and Vibration (2000) **234**(1), 115–134
doi:10.1006/jsvi.1999.2858, available online at http://www.idealibrary.com on IDEAL®

GALLOPING OF BUNDLE CONDUCTOR

Q. Zhang, N. Popplewell and A. H. Shah

Faculty of Engineering, The University of Manitoba, Winnipeg, Manitoba, Canada R3T 5V6

(*Received* 7 *July* 1997 *and in final form* 2 *December* 1999)

A useful design tool is developed for a bundle conductor of an electrical transmission line by using a three-degree-of-freedom hybrid model. The model is adaptable because it incorporates numerical mode shapes determined by numerically employing the finite element technique to form relevant matrices. On the other hand, it is quite computationally efficient because analytical expressions are used to investigate the initiation and steady state amplitudes of galloping. The model accommodates interactions of the vertical, horizontal and torsional movements, non-linear aerodynamic loads, a non-uniform ice geometry, distributed and discrete galloping control devices, and a variation of the wind along a span. By neglecting the sub-span motions between the conductors, a bundle is modelled as an equivalent single conductor so that the initiation conditions for galloping, periodic and quasi-periodic states and their stability conditions are considered by taking advantage of previous achievements for a single conductor. Numerical examples are presented to assess the accuracy of the results obtained from the model in comparison with analogous data from a more sophisticated finite element analysis. Parametric studies are reported for limit cycle amplitudes with variations of the critical wind speed, wind speed above the critical wind speed, static tension and span length.

1. INTRODUCTION

High-voltage transmission lines are often arranged in multi-conductors per phase to increase the power capacity of a circuit. They are often subjected to wind-induced vibrations. Galloping, which is a low-frequency, high-amplitude oscillation caused by a steady wind, happens more easily on a bundle conductor than on a single conductor [1]. Although considerable effort has been expended for many years to predict the galloping of a bundle conductor from that of a simpler single conductor, the extrapolation has still not been resolved satisfactorily. One reason is that existing analytical and computational models are either oversimplified or they lack the efficiency needed to economically compute the effects of design changes in parameters [2–4] like the static tension, the span length and the number of conductors in a bundle or the result of a greater wind speed.

Most previous analytical studies of bundle conductors have been limited to a planar configuration [5–10]. However, field observations indicate that galloping often involves the simultaneous interaction of a horizontal motion with vertical and torsional movements [1]. Although a three-degree-of-freedom (3d.o.f.) analytical model has been formulated recently for a bundle conductor [11], a tedious time-integration procedure was adopted and the aerodynamic forces were over simplified by their linearization. On the other hand, a more realistic, yet computationally efficient, 3d.o.f. model has been developed in the last decade to determine the initiation conditions for galloping as well as the ensuing dynamic limit cycle motion but only for a single conductor [12–15]. However, practically important non-uniformities arising, say, from icing variations or localized control devices like airflow

0022-460X/00/260115 + 20 $35.00/0

spoilers or detuning pendulums cannot be accommodated. The aim of this paper is to overcome this deficiency and extend the single conductor approach to a bundle configuration having any number of conductors. Therefore, an adaptable but still computationally efficient 3d.o.f. hybrid model is developed that uses finite element (FE) mode shapes, instead of their analytical counterparts, to construct the model and couple it to analytical expressions [15] to investigate the initiation and steady state amplitude of galloping.

Only the commonly occurring bulk motion of a bundle configuration [1] is studied in which all the conductors move in phase. Then it is only necessary to consider, in detail, a reference curve that fictitiously connects the mass centers of the bundle's cross-sections. In other words, the reference curve is analogous to a single conductor but its motion can be extrapolated to the individual conductors of a bundle. Predictions are compared with analogous data from a more sophisticated FE analysis. The latter uses time averaging rather than time integration to significantly reduce the still appreciable computational effort. Results from parametric studies are presented for critical wind speeds, which are important to the initiation of galloping, as well as for limit cycle amplitudes at different wind speeds, static tensions and span lengths.

2. HYBRID MODEL

Although an arbitrary number of conductors is considered, the particular example of a twin conductor bundle is illustrated in Figure 1 for simplicity. Figure 1(a) presents the static positions of the two conductors that are produced by the conductors' weights and tensions as well as by the steady (side) wind and the weight of accreted ice. A typical cross-section of the ith iced conductor (where $i = 1, 2$ for the twin bundle) is shown in Figure 1(b). Physical rigid spacers joining the conductors are illustrated as solid lines. Weightless, rigid fictitious spacers are introduced that periodically join the conductors to ensure that they essentially move together (i.e., the bulk motion constraint). Of course such spacers, which are represented in Figure 1(a) by dashed lines, are not needed for a single conductor. The reference curve for the bundle is considered to go through the mass center of each cross-section of the bundle, as indicated in Figure 1(a). On the other hand, adjacent spans are always idealized, as for the single conductor, by equivalent linear springs. Therefore, the principal difference between the single and bundle conductor approaches is the advancement of fictitious spacers and a reference curve for a bundle configuration.

The hybrid model makes the following assumptions in order to extend the single conductor formulation to a bundle conductor.
(1) Inertial and damping forces in the longitudinal direction, as well as the rotation of individual conductors about this direction, are neglected. (2) A line's sag-to-span ratio is small. (3) The rotation of the bundle about the reference curve is small and spacers are rigid. (4) No more than one mode per global direction is considered simultaneously. (5) The relative motions between the conductors of a bundle are neglected and the longitudinal motions of each of the conductors are presumed to be identical.

Items (1), (2) and (5) are the commonly made assumptions for the bulk motion of a bundle. The third item is reasonable in many cases because a bundle's torsional stiffness is much greater than that of a single conductor so that large rotations happen rarely. Item (4), on the other hand, presumes that the larger torsional stiffness of a bundle hardly changes the negligible coupling that is assumed for the single conductor for modes acting in the same direction. These simplifying assumptions are used next to formulate the hybrid model.

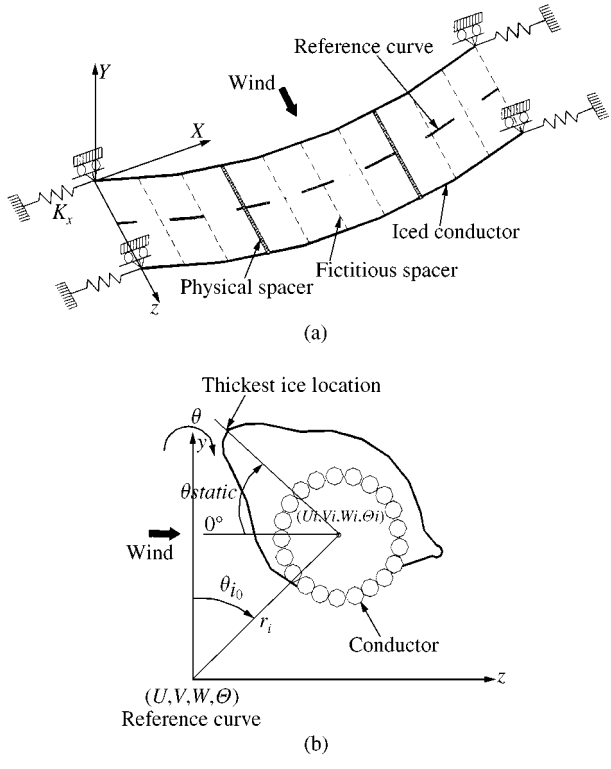

Figure 1. Showing (a) the bulk modelling of a twin bundle conductor, and (b) the cross-section of the *i*th iced conductor.

2.1. DISPLACEMENT RELATIONSHIP

The dynamic displacement at an arbitrary point (s, y, z) of any one conductor in a bundle is measured from that point's static position. It is given by

$$u_X(s, y, z, t) = U(s, t), \qquad v_Y(s, y, z, t) = V(s, t) - z\Theta(s, t), \qquad w_Z(s, y, z, t) = W(s, t) + y\Theta(s, t). \tag{1}$$

X, Y and Z are the global co-ordinates illustrated in Figure 1(a) while x, y and z are the local co-ordinates shown in Figure 1(b). The latter are off-set from the global co-ordinates and their origin is located on the reference curve at the left support. u_X, v_Y and w_Z are the global displacements at (s, y, z) and instant t. Their direction is indicated by the corresponding suffix. On the other hand, s is the intrinsic co-ordinate which indicates the distance that a cross-section of the bundle is from the reference curve's origin. U, V and W are the global displacements of any point of the reference curve in the X, Y and Z directions respectively. Θ is the rotation of the bundle about the reference curve and it is assumed to be small. If only one mode is considered in each direction, then U, V, W and Θ can be expressed as

$$U(s, t) = q_u(t) f_u(s), \qquad V(s, t) = q_v(t) f_v(s), \qquad W(s, t) = q_w(t) f_w(s), \qquad \Theta(s, t) = q_\theta(t) f_\theta(s). \tag{2}$$

The q_i and f_i, where $i = u, v, w, \theta$, are generalized co-ordinates and the associated mode shapes provided by the FE model, respectively (see Section 3). Furthermore,

the displacements of the center of the ith conductor in the bundle, U_i, V_i and W_i, are described by

$$U_i(s, y, z, t) = U(s, y, z, t), \qquad V_i(s, y, z, t) = V(s, t) - r_i \sin\theta_{i0}\Theta(s, t),$$

$$W_i(s, y, z, t) = W(s, t) + r_i \cos\theta_{i0}\Theta(s, t). \tag{3}$$

Here r_i is the distance between the reference curve and the center of the ith bare conductor at the bundle's cross-section of interest. Moreover, θ_{i0} is the initial clockwise angle of this conductor from the positive direction of the y-axis, as illustrated in Figure 1(b).

2.2. EQUATIONS OF MOTION

The equations of motion of the bundle are found by employing the conventional variational principle [16], i.e.,

$$\int_{t_1}^{t_2} \delta(T_k - V_s)\,\mathrm{d}t + \int_{t_1}^{t_2} \delta W_{nc}\,\mathrm{d}t = 0, \tag{4}$$

where T_k and V_s are the total kinetic and strain energies respectively. W_{nc} is the work done by the non-conservative forces and δ indicates the first order variation. By neglecting the inertial effects in the longitudinal direction, T_k is given by

$$T_k = \frac{1}{2}\int_0^L \int_{A_T} \rho(\dot{v}_Y^2 + \dot{w}_Z^2)\,\mathrm{d}A\,\mathrm{d}s + \frac{1}{2}\sum_{k=1}^{p} [m_{sk}V^2(s_k, t) + m_{sk}W^2(s_k, t) + I_{sk}\Theta^2(s_k, t)], \tag{5}$$

where L is the total length of a line in a span, ρ is the mass density of the iced bundle conductors' total cross-sectional area A_T, m_{sk} and I_{sk} are the mass and the mass moment of inertia of the kth spacer, respectively, s_k is the intrinsic co-ordinate of the kth spacer's intersection with the reference curve, p is the number of spacers, and a dot superscript indicates differentiation with respect to time, t. The variation of the strain energy for a bundle's bulk motion, δV_s, can be obtained by summing the strain energies of each of its conductors [15, 17], i.e.,

$$\delta V_s = \sum_{i=1}^{n} \int_0^L [AE\delta\varepsilon_s\varepsilon_s + B_T(\delta\varepsilon_s\varepsilon_\theta + \varepsilon_s\delta\varepsilon_\theta) + GJ\delta\varepsilon_\theta\varepsilon_\theta + T\delta\varepsilon_s + M_t\delta\varepsilon_\theta]_i\,\mathrm{d}s. \tag{6}$$

Suffix i in equation (6) represents the ith conductor again and n is the total number of conductors in a bundle. ε_s is the Lagrangian strain of the ith conductor, along s, such that

$$\varepsilon_s = \frac{\partial x}{\partial s}\frac{\partial u_X}{\partial s} + \frac{\partial y}{\partial s}\frac{\partial V_i}{\partial s} + \frac{\partial z}{\partial s}\frac{\partial W_i}{\partial s} + \frac{1}{2}\left[\left(\frac{\partial u_X}{\partial s}\right)^2 + \left(\frac{\partial V_i}{\partial s}\right)^2 + \left(\frac{\partial W_i}{\partial s}\right)^2\right]. \tag{7}$$

On the other hand, the torsional strain of a conductor, ε_θ, can be expressed as

$$\varepsilon_\theta(s) = \frac{\partial\Theta(s)}{\partial s}. \tag{8}$$

T in equation (6) is the static tension in each conductor, M_t is a conductor's initial internal twisting moment that resists the external moment caused by an eccentric ice weight, A and

GJ are the cross-sectional area and the torsional rigidity of a bare conductor, respectively, E is the modulus of elasticity and B_T represents an axial-torsional coupling [18].

The variation of the virtual work is described by

$$\delta W_{nc} = \int_0^L [F_y(s)\delta V + F_z(s)\delta W + F_\theta(s)\delta\Theta]\,\mathrm{d}s - \delta\mathbf{q}_a^{\mathrm{T}}\mathbf{C}_a^{\mathrm{T}}\dot{\mathbf{q}}_a. \tag{9}$$

F_y, F_z and F_θ are the aerodynamic loads (per unit span length of the bundle) which act at the reference curve in the y, z and θ directions respectively. $\mathbf{C}_a$ is an experimentally found damping matrix that takes the form

$$\mathbf{C}_a = \begin{bmatrix} 0 & \mathbf{0}_3 \\ \mathbf{0}_3^{\mathrm{T}} & \mathbf{C} \end{bmatrix}, \tag{10}$$

where $\mathbf{0}_3$ is the 1×3 null matrix. On the other hand, the elements of the diagonal matrix $\mathbf{C}$ are

$$c_{11} = 2\omega_y\xi_y m_{11}, \qquad c_{22} = 2\omega_z\xi_z m_{22}, \qquad c_{33} = 2\omega_\theta\xi_\theta m_{33}. \tag{11}$$

$\omega_i\,(i = y, z, \theta)$ and $\xi_i\,(i = y, z, \theta)$ are, respectively, the bundle's undamped, uncoupled natural frequencies and the measured damping ratios associated with the uncoupled vibrations in the direction indicated by a subscript. m_{ii} are the elements of the matrix $\mathbf{M}$ defined in equation (14). Finally, $\mathbf{q}_a$ in equation (9) is defined by

$$\mathbf{q}_a^{\mathrm{T}} = (q_u\ \mathbf{q}^{\mathrm{T}}), \quad \textit{where}\ \mathbf{q}^{\mathrm{T}} = (q_v\ q_w\ q_\theta). \tag{12}$$

Substituting equations (5)–(12) into equation (4) yields the equations of motion as

$$\mathbf{M}_a\ddot{\mathbf{q}}_a + \mathbf{C}_a\dot{\mathbf{q}}_a + \mathbf{K}_a\mathbf{q}_a = \mathbf{F}_a, \tag{13}$$

where $\mathbf{M}_a$ and $\mathbf{K}_a$ are a 4×4 mass matrix and stiffness matrix respectively. $\mathbf{M}_a$ takes the form

$$\mathbf{M}_a = \begin{bmatrix} 0 & \mathbf{0}_3 \\ \mathbf{0}_3^{\mathrm{T}} & \mathbf{M} \end{bmatrix} \tag{14}$$

and the non-zero elements of $\mathbf{M}$ and $\mathbf{K}_a$ are given more conveniently in Appendix A. The aerodynamic load vector, $\mathbf{F}_a$, in equation (13) is found at the reference curve from aerodynamic data measured at the centers of the individual conductors of a bundle. It is represented as

$$\mathbf{F}_a^{\mathrm{T}} = (0\ \mathbf{F}^{\mathrm{T}}). \tag{15}$$

The components of $\mathbf{F}^{\mathrm{T}} = (F_y\ F_z\ F_\theta)$ are expressed conventionally as non-linear functions of the wind's angle of attack α, the conductor's diameter d, side wind speed U_z, and the density of air, ρ_{air}. In an analogous fashion to a single conductor, they are approximated in Appendix A as cubic polynomials in α where

$$\alpha = \Theta - \frac{d}{2U_z}\dot{\Theta} - \frac{\dot{V}}{U_z} \tag{16}$$

by assuming that

$$\tan^{-1}\left(\frac{d}{2U_z}\dot{\Theta} + \frac{\dot{V}}{U_z}\right) \simeq \frac{d}{2U_z}\dot{\Theta} + \frac{\dot{V}}{U_z} \tag{17}$$

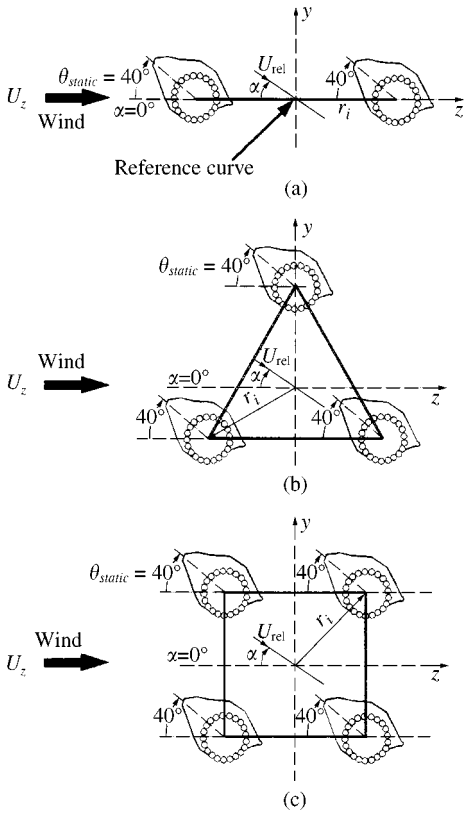

Figure 2. The initial arrangement of iced C11 conductors in (a) a twin bundle, (b) triple bundle and (c) quad bundle configuration.

and approximating the characteristic radius [12] by $d/2$. The major difference for a bundle conductor is that the reference curve is used to define α rather than the single conductor itself (see, for example, Figure 2). It is assumed, for simplicity, that the aerodynamic interactions between the different conductors of a bundle are negligible. This assumption appears intuitively more reasonable for wider separations of the conductor. For example, it seems increasingly plausible when the separation between the conductors of a twin bundle is enlarged beyond 10 conductor diameters [19]. Then the aerodynamic forces and moments measured for an individual conductor can be merely summed at the reference curve. Details of the basic aerodynamic loads considered here are given in reference [15]. They correspond to the single iced conductor illustrated in Figure 1(b).

The equations of motion for the condensed 3d.o.f. system are obtained from equation (13) by partitioning $\mathbf{K}_a$ so that

$$\mathbf{K}_a = \begin{bmatrix} k_{11} & \mathbf{K}_2 \\ \mathbf{K}_2^{\mathrm{T}} & \mathbf{K}_3 \end{bmatrix}. \tag{18}$$

By eliminating the terms associated with the axial displacements, equation (13) becomes

$$\mathbf{M}\ddot{\mathbf{q}} + \mathbf{C}\dot{\mathbf{q}} + \mathbf{K}\mathbf{q} = \mathbf{F}, \tag{19}$$

where

$$\mathbf{K} = \mathbf{K}_3 - \mathbf{K}_2^{\mathrm{T}} k_{11}^{-1} \mathbf{K}_2. \tag{20}$$

3. FINITE ELEMENT MODEL

Consider a bundle consisting of n conductors. Each conductor is considered to have n_p nodes. The jth nodes of all the conductors are assumed to be connected either by a physical or a ficticious, rigid spacer. In the FE formulation, the relevant mass, stiffness and damping matrices as well as the nodal force vector are formulated for each conductor of the bundle. These equations are transformed to the reference curve with the help of the physical or ficticious rigid spacers.

All but two of the assumptions used to develop the hybrid model are utilized in the FE modelling of a bundle conductor. The exceptions avoid the neglect of the longitudinal inertias and the assumption of solely a single mode acting in a specified direction. Details of the FE formulation have been given previously for a single conductor [20]. As before, a conductor is represented by employing three node, isoparametric cable elements. After forming the equations of motion for each conductor, transforming them to the reference curve and assembling the matrices, the final equations take the form

$$[M]\{\ddot{q}\} + [C]\{\dot{q}\} + [K]\{q\} = \{F\}, \tag{21}$$

where

$$[M] = \sum_{i=1}^{n} [T^{(i)}]^{\mathrm{T}}[M^{(i)}][T^{(i)}] + [M_s], \qquad [C] = \sum_{i=1}^{n} [T^{(i)}]^{\mathrm{T}}[C^{(i)}][T^{(i)}],$$

$$[K] = \sum_{i=1}^{n} [T^{(i)}]^{\mathrm{T}}[K^{(i)}][T^{(i)}], \qquad \{F\} = \sum_{i=1}^{n} [T^{(i)}]^{\mathrm{T}}\{F^{(i)}\},$$

$$\{q\} = \{\{q_1\}^{\mathrm{T}}, \{q_2\}^{\mathrm{T}}, \ldots, \{q_{n_p}\}^{\mathrm{T}}\}^{\mathrm{T}}, \qquad \{q_j\}^{\mathrm{T}} = (U_j^{(i)}, V_j^{(i)}, W_j^{(i)}, \Theta_j^{(i)}). \tag{22}$$

$U_j^{(i)}$, $V_j^{(i)}$ and $W_j^{(i)}$ are the global displacements of node j of the reference curve and $\Theta_j^{(i)}$ is the rotation of the bundle about the reference curve. The $[M^{(i)}]$, $[C^{(i)}]$ and $[K^{(i)}]$, $i = 1, 2, \ldots, n$, are, respectively, the mass, damping and stiffness matrices of size $4n_p \times 4n_p$. $\{F^{(i)}\}$ is the corresponding load vector of size $4n_p \times 1$. The construction of these matrices is given in reference [20]. $[T^{(i)}]$ is a 4×4 transformation matrix whose non-zero elements are $T_{11} = T_{22} = T_{33} = T_{44} = 1$, $T_{24} = r_i \cos\theta_{i0}$, and $T_{34} = r_i \sin\theta_{i0}$. Again, r_i is the distance between the reference curve and the center of the ith bare conductor and θ_{i0} is the initial clockwise angle of this conductor as viewed from the positive direction of the y-axis; see Figure 1(b). If the Delta function, δ_{sj}, is denoted by

$$\delta_{sj} = \begin{cases} 0 & \text{for a massless, fictitious spacer introduced at node } j, \\ 1 & \text{for a physical spacer having an end at node } j, \end{cases} \tag{23}$$

then the diagonal mass matrix, $[M_s]$, in equation (22), which represents the contribution from the physical spacers' inertias, can be written as

$$[M_s] = \begin{bmatrix} \delta_{s1}M_{s1} & 0 & & \cdots & 0 \\ 0 & \delta_{s2}M_{s2} & 0 & \cdots & 0 \\ \vdots & \ddots & \ddots & \ddots & \vdots \\ 0 & \cdots & 0 & \delta_{s(n_p-1)}M_{s(n_p-1)} & 0 \\ 0 & \cdots & & 0 & \delta_{sn_p}M_{sn_p} \end{bmatrix}. \tag{24}$$

The diagonal matrix $[M_{sj}]$ is given by

$$[M_{sj}] = \begin{bmatrix} m_{sj} & 0 & 0 & 0 \\ 0 & m_{sj} & 0 & 0 \\ 0 & 0 & m_{sj} & 0 \\ 0 & 0 & 0 & I_{sj} \end{bmatrix}, \tag{25}$$

where m_{sj} and I_{sj} are the mass of the physical spacer and its mass moment of inertia about the reference curve at node j respectively. Note that the mode shapes, $f_u(s)$, $f_v(s)$, $f_w(s)$ and $f_\theta(s)$ in equation (2) are taken in the discretized form

$$(f_u, f_v, f_w, f_\theta) = (U^i, V^i, W^i, \Theta^i). \tag{26}$$

4. STABILITY ANALYSIS AND LIMIT CYCLES

Steps involved in the stability analysis of the static configuration and the determination of the limit cycles are detailed in reference [15] for the hybrid model or in reference [21] for the FE model. Hence, only a brief description is given here.

The first step in determining the feasibility of galloping is to investigate whether the initial equilibrium solution (IES) of the linearized form of equation (19) or equation (21) is stable. If all the eigenvalues of the homogeneous equation (19) or equation (21) have a negative real part, then the static configuration is asymptotically stable and a further analysis is not required. If, however, at least one of the eigenvalues crosses the real axis (a critical point) when a parameter changes, say an increasing wind speed U_z, then the IES becomes unstable and galloping may be initiated. The critical wind speed, U_{zc}, is the value at which the IES just becomes unstable. Once the IES becomes unstable, new equilibrium states or dynamic motions, which are periodic or quasi-periodic, may emerge from the critical point. (Note that chaotic states are not investigated.) Perturbation techniques are employed to study the dynamic motions and to find the limit cycles' amplitudes. Explicit expressions to determine the IES and the limit cycles' amplitudes are given in reference [15] for the hybrid model. On the other hand, a step-by-step procedure is given in reference [21] for computing the dynamic motion using the FE model.

5. NUMERICAL RESULTS

A trend analysis that arises from changes in key parameters like the horizontal tension of a conductor, span length, structural damping, critical wind speed, wind speed above critical wind speed, etc. is important for engineers. Therefore, numerical results focus on the effects of a bundle's parameters on galloping.

The examples considered here assume that the iced conductors have simple end supports which permit longitudinal degrees of freedom so that a more realistic interaction can be accommodated between adjacent spans. Ice accumulations on the conductors, whose asymmetry may cause the conductors' instability, are obtained from a single conductor sample placed in a freezing rain simulator [19]. The resulting (C11) cross-section is illustrated in Figure 2. It resembles the D form used traditionally to induce galloping in field trials [22]. This particular ice formation is assumed to be accreted identically on each conductor. In other words, variations in the ice shape that could arise from one conductor partially shielding another conductor from the wind are ignored for simplicity. The wind speed is also presumed to be constant along the span.

5.1. NATURAL FREQUENCIES AND LIMIT CYCLES

Limit cycle amplitudes, mainly the components in the vertical and horizontal directions, are important in avoiding an electrical flashover or the clashing of conductors. They are related not only to the aerodynamic loads but also to the natural frequencies of the conductors. In particular, natural frequencies determine if an internal resonance happens which, in turn, crucially affects the dynamic behavior of the conductors. An internal resonance occurs when the ratio of at least two of the natural frequencies is close to a ratio of two positive integers. The parameters in Table 1 are selected so that the lowest horizontal mode participates in an internal resonance. In this table, I is the centroidal inertial moment of the bare conductor; e_y and e_z represent the eccentricity in the y and z directions respectively. A_{ice} is a total cross-sectional area of the iced conductor and m is the corresponding mass per unit length. Table 2 gives a comparison of the lowest three natural frequencies of various bundles and a single conductor in plunge (vertical), swingback (horizontal) and torsion that are predicted by the hybrid and FE models. The finite element model has 21 nodes along the reference curve where numbers 1 and 21 represent the left and right supports, respectively, and 19 fictitious spacers are always used for all bundle configurations.

Table 2 indicates that the percentage differences between the natural frequencies produced by the hybrid and FE models are within an acceptable 1%. The natural frequencies corresponding to a plunge (vertical) or swingback (horizontal) motion are almost the same for a given number of loops per span, regardless of the number of conductors. This behavior occurs because the mass and stiffness in these directions change almost identically with an increasing number of conductors. The torsional frequencies, on the other hand, decrease noticeably as more conductors are added because the change in the moment of inertia is greater than that for the stiffness. Identical trends have also been observed from existing bundle models [23, 11].

The hybrid and finite element models are employed to investigate the dynamic limit cycle amplitudes. From a practical viewpoint, one through three loops per span are usually considered in North America because they are most frequent for galloping [1]. The examples in this paper, however, only consider the mid-span and quarter span results for one and two loops per span galloping, respectively, because the limit cycle amplitudes for the three loops per span case are invariably much smaller. The initial placements of the different bundle configurations are shown in Figure 2. The corresponding aerodynamic coefficients, a_{ij}, are given in Table 3 for $\theta_{static} = 40^\circ$ and $\theta_{static} = 270^\circ$. Both the hybrid and finite element models predict that, regardless of the number of conductors in a bundle, the

TABLE 1

Iced C11 line properties

Parameter	Data	Parameter	Data
d (m)	0·0286	A (mm^2)	423·24
E (N/m^2)	$4{\cdot}78033 * 10^{10}$	m (kg/m)	2·379
GJ (N m^2/rad)	101	ξ_y, ξ_z	$0{\cdot}515 * 10^{-3}$
I (kg m)	$0{\cdot}3334 * 10^{-3}$	ξ_θ	0·308
H (N)	30000	r_i (m)	0·2355
e_y (mm)	2·05	L_x (m)	125·88
e_z (mm)	−0·63	ρ_{air} (kg/m^3)	1·2929
A_{ice} (mm^2)	594·48	U_z (m/s)	4·0

TABLE 2

Comparison of natural frequencies ($L_x = 126$ m, $H = 30$ kN)

Number of conductors	No. of loops/span	1			2			3		
	Natural frequencies (Hz)	ω_y	ω_z	ω_θ	ω_y	ω_z	ω_θ	ω_y	ω_z	ω_θ
1	HM	0·482	0·445	1·091	0·891	0·892	4·003	1·337	1·339	6·384
	FM	0·482	0·444	1·090	0·891	0·891	4·003	1·339	1·337	6·385
2	HM	0·482	0·443	0·635	0·892	0·893	1·174	1·341	1·347	1·737
	FM	0·482	0·446	0·635	0·892	0·892	1·174	1·340	1·339	1·737
3	HM	0·482	0·443	0·555	0·892	0·893	1·062	1·341	1·347	1·581
	FM	0·481	0·446	0·555	0·891	0·892	1·062	1·340	1·338	1·581
4	HM	0·481	0·443	0·553	0·892	0·893	1·060	1·341	1·347	1·578
	FM	0·481	0·446	0·553	0·891	0·892	1·060	1·340	1·338	1·578

Note: HM—hybrid model; FM—finite element model.

initial equilibrium state is unstable at the assumed 4 m/s wind speed (i.e., the stability criterion is first violated [15]). A $1:1:0$ ($\omega_y:\omega_z:\omega_\theta$) resonant galloping occurs in a one loop per span motion for the single as well as for the bundle conductors. In addition, a $1:1:1$ resonant galloping can occur but only for a two loops per span motion of the bundle conductors. Figures 3(a) and (b) compare the resulting bulk motion limit cycles for one and two loops per span motions respectively. The results from the hybrid model agree with the FE predictions. The A_y and A_z used in this figure correspond to the vertical and horizontal limit cycle amplitudes for the single conductor or the reference curve of a bundle. It can be seen from Figure 3(a) that the vertical amplitudes for the one loop per span case are invariably comparable in magnitude. They are much greater than the horizontal displacements for the bundle conductors so that the plunge motion dominates the one loop per span galloping for the bundles. Therefore, it is not surprising that a predominantly vertical conductor motion has a high percentage of occurrence in the field [1]. On the other hand, Figure 3(b) suggests that the horizontal motion is comparable or larger in magnitude to that of the plunge for a two loops per span oscillation. Therefore, the horizontal motion should not be neglected in such cases.

5.2. CRITICAL AND HIGHER WIND SPEED TRENDS

Two static angles of attack, $\theta_{static} = 40$ or 270°, are selected to illustrate that the classical Den Hartog criterion, which depends only upon the aerodynamic characteristics of the conductors, does not necessarily give the initiation of galloping. According to this criterion, an instability occurs when $\partial C_L/\partial\alpha + C_D < 0$. C_L and C_D are purely the aerodynamic lift and drag coefficients, respectively, which are defined in Appendix A. The previously considered single and bundle conductors are used again to determine how the ensuing dynamic limit cycle amplitude changes with the critical wind speed and an increasing steady side wind speed beyond this critical value.

Figure 4 shows the variation in the reduced critical wind speed, $\bar{U}_{zc} = U_{zc}/fL_x$, and the non-dimensional limit cycle amplitude, $\bar{A} = \sqrt{A_y^2 + A_z^2}/s_a$, at the static angle of attack

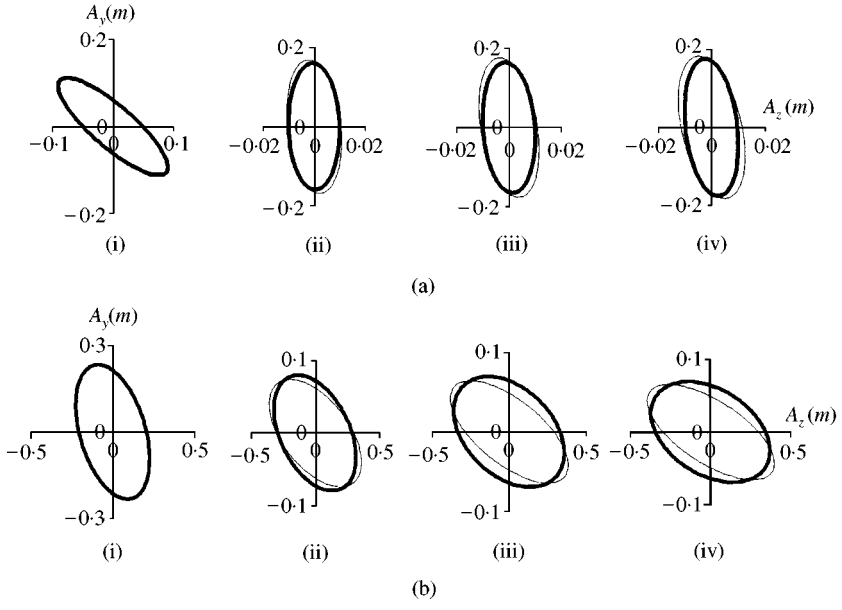

Figure 3. Limit cycle obtained at (a) the mid-span (1 loop/span) and (b) quarter-span (2 loops/span) for (i) a single conductor, (ii) twin bundle, (iii) triple bundle, and (iv) a quad bundle (span length $L_x = 125{\cdot}88$ m, horizontal static tension $H = 30$ kN, side wind speed $U_z = 4$ m/s, $\alpha = 0^\circ$ and $\theta_{static} = 40^\circ$): —, Hybrid model; —, FE model.

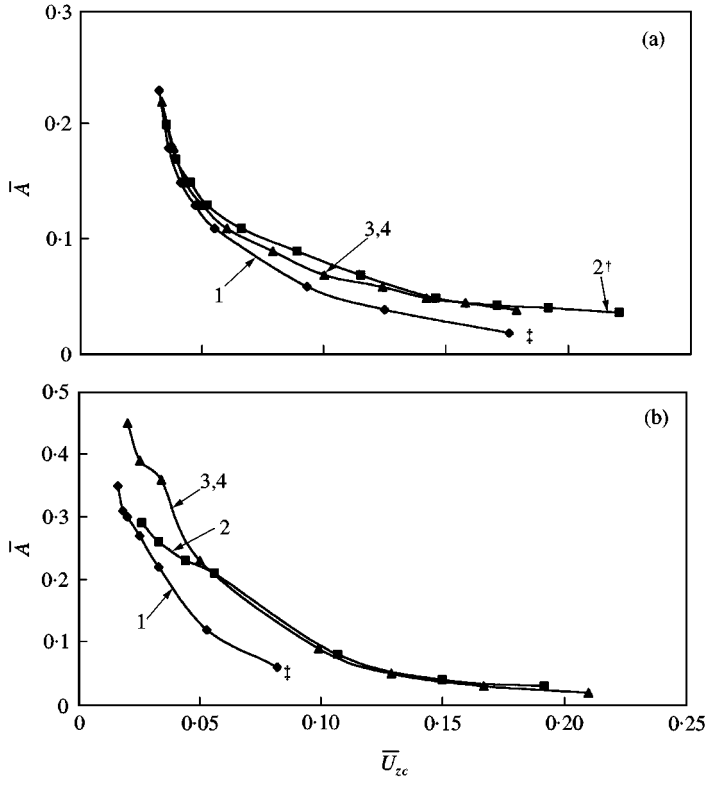

Figure 4. Limit cycle amplitude ratio, $\bar{A}$, at different critical wind speed ratios, $\bar{U}_{zc}$, for (a) one loop/span and (b) two loops/span galloping ($\theta_{static} = 40^\circ$, $\alpha = 0^\circ$). †, Number of conductors (in a bundle); ‡, stable at higher values of $\bar{U}_{zc}$.

$\theta_{static} = 40°$. (Note that this particular angle is illustrated in both Figures 1(b) and 2.) The f is the lowest ω_y, the predominantly vertical natural frequency, L_x is the horizontal span length, and s_a is the static sag at a line's mid-span. The figure indicates that $\bar{A}$ invariably decreases as $\bar{U}_{zc}$ increases, immaterial of the number of loops per span and regardless of the number of conductors in a bundle. However, the single conductor always has the lowest $\bar{A}$ at a given $\bar{U}_{zc}$. On the other hand, the vertical amplitude, A_y, always dominates $\bar{A}$ in Figure 4(a) while A_z is the principal component of $\bar{A}$ in Figure 4(b). Figure 5 presents analogous results to Figure 4(a) for $\theta_{static} = 270°$. Only data for the single conductor is

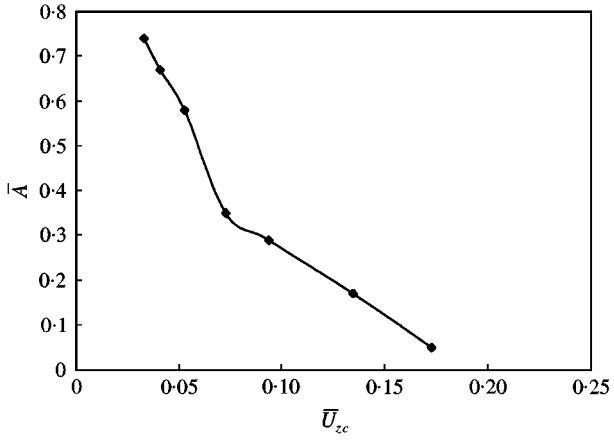

Figure 5. Limit cycle amplitude ratio, $\bar{A}$, at different critical wind speed ratios, $\bar{U}_{zc}$, for one loop/span galloping of the single conductor ($\theta_{static} = 270°$).

TABLE 3

Aerodynamic coefficients for C11

Number of conductors in bundle	Coefficients at $\alpha = 0°$ and $\theta_{static} = 40°$			
	i	a_{yi}	a_{zi}	$a_{\theta i}$
Single conductor	1	−0·1667	0·8605	−0·7272
	2	−4·0547	0·8325	0·2935
	3	8·3581	1·7815	5·9704
2	1	−0·3335	1·7210	−1·4543
	2	−8·1094	1·6650	0·5869
	3	16·7162	3·5631	11·9408
3	1	−0·5003	2·5815	−2·1815
	2	−12·1614	2·4975	0·8804
	3	25·0743	5·3447	17·9112
4	1	−0·6670	3·4420	−2·9086
	2	−16·2188	3·3300	1·1738
	3	33·4324	7·1262	23·8816
	Coefficients at $\theta_{static} = 270°$			
Single conductor	1	0·9423	1·3186	−0·8567
	2	−0·9245	−3·2000	0·9026
	3	2·6352	−13·0623	−0·2353

shown in Figure 5 because the bundle conductors are invariably stable when $\theta_{static} = 270°$. The major difference from Figure 4(a) is that the Den Hartog criterion is satisfied no longer for the single conductor. (Table 3 indicates that $\partial C_L/\partial\alpha + C_D$ is negative at $\theta_{static} = 40°$ but positive at $\theta_{static} = 270°$.) Despite this difference, the single conductor remains

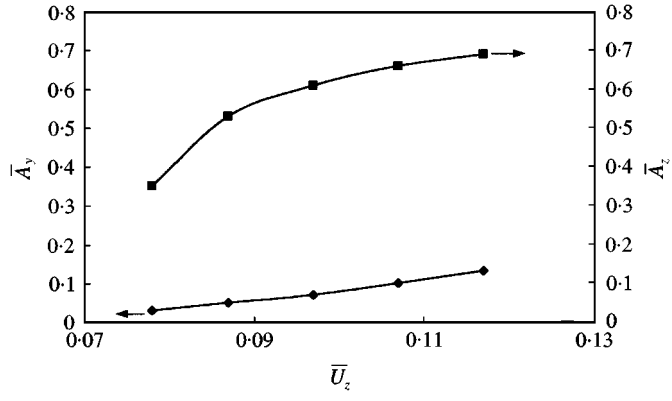

Figure 6. Limit cycle amplitude ratios, $\bar{A}_y$ and $\bar{A}_z$, at different wind speed ratios, $\bar{U}_z$, for one loop/span galloping of the single conductor ($\theta_{static} = 270°$).

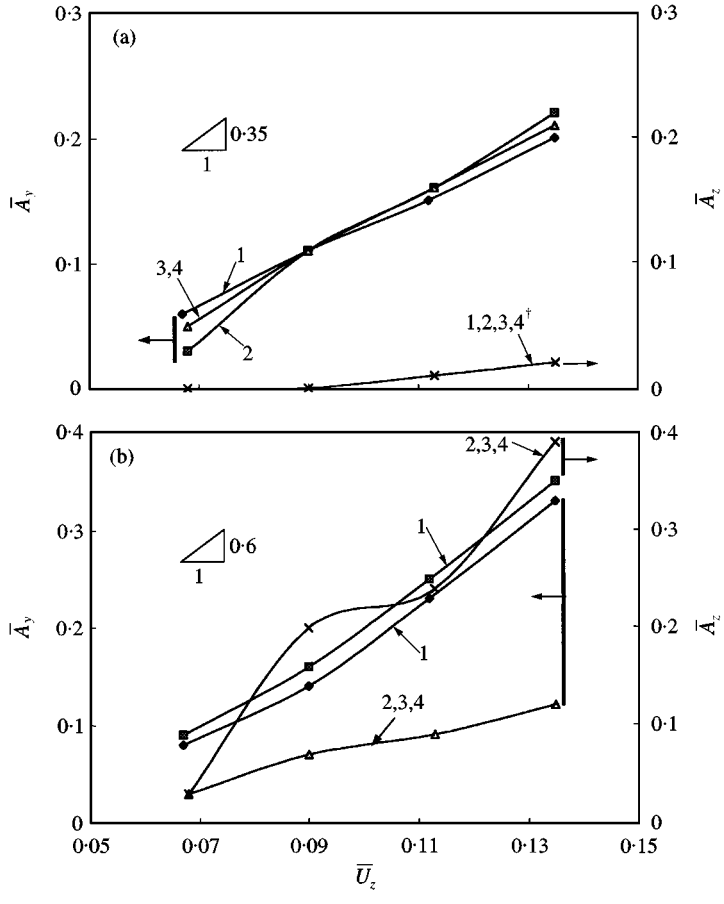

Figure 7. Limit cycle amplitude ratios, $\bar{A}_y$ and $\bar{A}_z$, at different wind speed ratios, $\bar{U}_z$, for (a) one loop/span galloping and (b) two loops/span galloping. †Notation as in Figure 4 ($\alpha = 0°$, $\theta_{static} = 40°$).

unstable—otherwise there would be no limit cycle amplitudes in Figure 5! Clearly, the simple Den Hartog criterion is not always applicable. On the other hand, $\bar{A}$ decreases again with increasing $\bar{U}_{zc}$, albeit more rapidly at the lowest $\bar{U}_{zc}$.

Figures 6 and 7 give the changes in the component non-dimensional limit cycle amplitudes, $\bar{A}_y$ and $\bar{A}_z$, as the steady wind speed rises above the reduced critical wind speed, $\bar{U}_{zc}$, for $\theta_{static} = 270^\circ$ and 40° respectively. In these figures, the static horizontal tension is $H = 30$ kN, the span length is $L_x = 126$ m, $\bar{U}_z = U_z/fL_x$, $\bar{A}_y = A_y/s_a$ and $\bar{A}_z = A_z/s_a$. The wind speed, U_z, varies from a steady 4 m/s to a steady 6 m/s. Not surprisingly, both $\bar{A}_y$ and $\bar{A}_z$ always grow as $\bar{U}_z$ and, hence, the wind's energy input to a line increases. As before, $\bar{A}_y$ is invariably much larger than $\bar{A}_z$ for one loop per span galloping and usually *vice versa* for two loops per span. The single conductor is the exception in the latter situation because the internal resonance and, hence, the coupling between the torsional and vertical or horizontal movements does not change. On the other hand, when galloping occurs, the number of conductors in a bundle hardly affects $\bar{A}_y$ and $\bar{A}_z$.

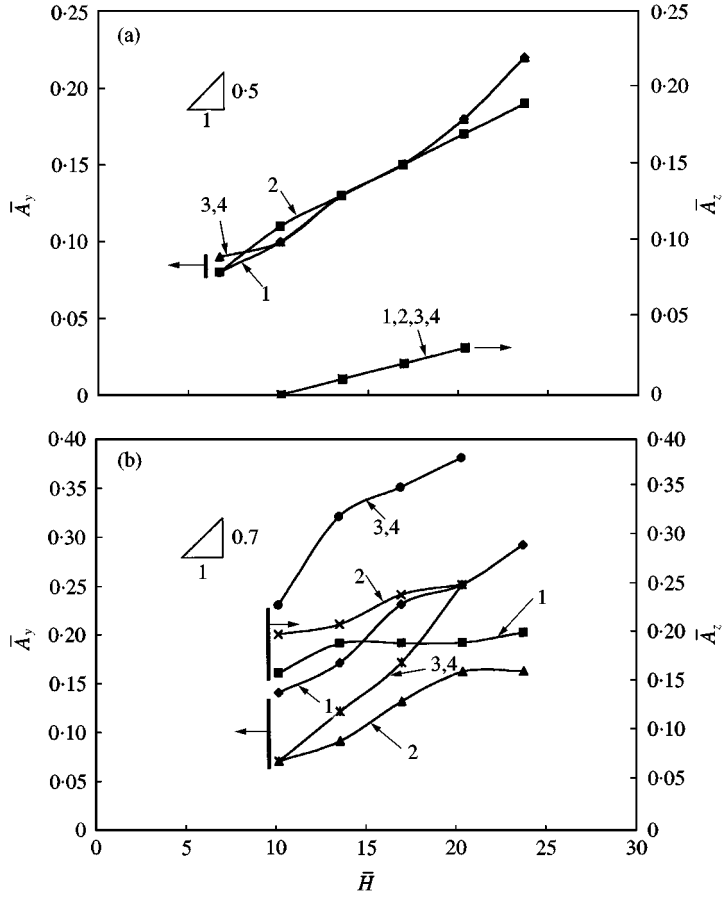

Figure 8. Limit cycle amplitude ratios, $\bar{A}_y$ and $\bar{A}_z$, at various horizontal tension ratios, $\bar{H}$, for (a) one loop/span galloping and (b) two loops/span galloping. Horizontal span length, L_x, is invariably 126 m ($\alpha = 0^\circ$, $\theta_{static} = 40^\circ$).

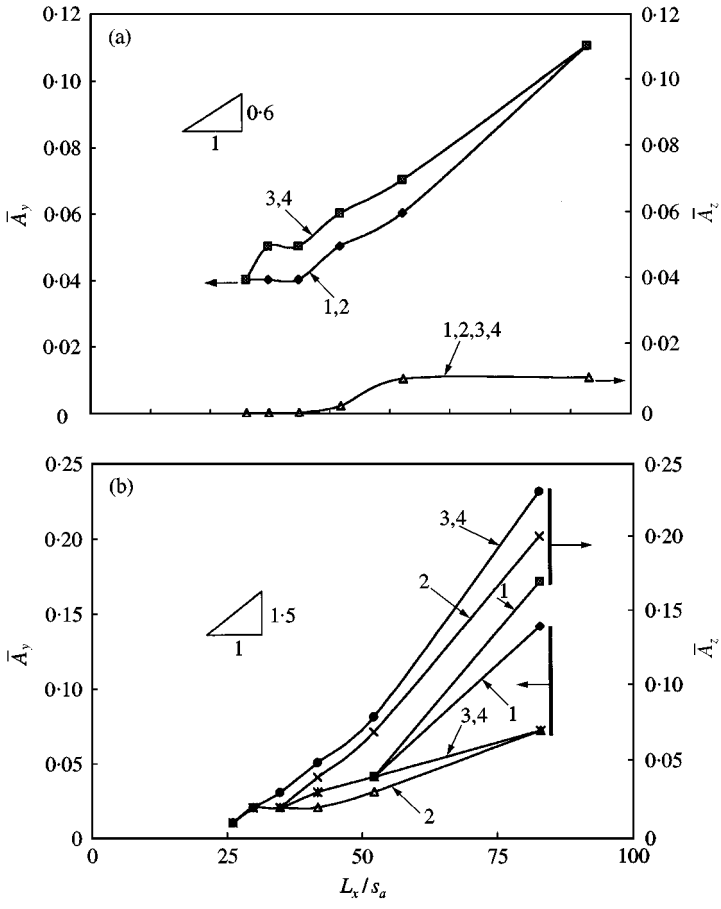

Figure 9. Limit cycle amplitude ratios, $\bar{A}_y$ and $\bar{A}_z$, at various span length ratios, L_x/s_a, for (a) one loop/span galloping (b) two loops/span galloping. Horizontal static tension, H, is always 30 kN ($\alpha = 0°$, $\theta_{static} = 40°$).

5.3. TRENDS FOR STATIC HORIZONTAL TENSION AND SPAN LENGTH

The effects on $\bar{A}_y$ and $\bar{A}_z$ of increasing the non-dimensional static horizontal tension, $\bar{H} = H/w$, and span length, L_x/s_a, are given in Figures 8 and 9, respectively, for $\theta_{static} = 40°$. Here w is the total weight of a bare conductor in one span. Both $\bar{A}_y$ and $\bar{A}_z$ invariably tend to grow as either $\bar{H}$ or L_x/s_a increases. The single loop per span case (Figures 8(a) and 9(a)) is little different to the comparable situation observed in Figure 7(a) for increasing $\bar{U}_z$. However, unlike before, the twin bundle has somewhat smaller $\bar{A}_y$ and $\bar{A}_z$ than the triple and quad bundles in two loops per span galloping, especially for enlarged $\bar{H}$. This difference is caused likely by the different torsional coupling to these components that arise from the appreciably smaller rotation of the twin bundle at higher $\bar{H}$.

6. CONCLUSIONS

A flexible and computationally efficient design tool is developed for bundle conductors. Results for a particular ice shape suggest that the ratio of the limit cycle amplitude to the mid-span's static sag invariably decreases as the critical wind speed ratio increases,

regardless of the number of loops per span considered or the number of conductors in a bundle. It also usually grows as the non-dimensional side wind speed (above the critical value), horizontal tension or span length increase—again, immaterial of the number of conductors. Den Hartog's criterion for the initiation of galloping is shown to be overly simplified.

ACKNOWLEDGMENT

The writers gratefully acknowledge the financial support of Manitoba Hydro and the Natural Sciences and Engineering Research Council of Canada. The computer programs provided by Drs P. Yu, Y. M. Desai and M. Liao for a single conductor are also appreciated greatly.

REFERENCES

1. Transmission Line Reference Book 1979 *EPRI*, *Palo Alto*, *CA*. Wind-induced conductor motion.
2. A. Simpson 1974 *Journal of Sound and Vibration* **20**, 417–449. Determination of the natural frequencies of multiconductor overhead transmission lines.
3. G. Diana, F. Cheli, A. Manenti, P. Nicolini and F. Tavano 1990 *IEEE Transaction on Power Delivery* **5**, 1910–1919. Oscillation of bundle conductors in overhead lines due to turbulent wind.
4. K. E. Gawronski 1977 *Ph.D. thesis*, *Clarkson College of Technology*. Non-linear galloping of bundle-conductor transmission lines.
5. A. S. Richardson 1981 *Proceedings of the IEEE* **128** (P*art C*), 211–218. Dynamic analysis of lightly iced conductor galloping in two degrees of freedom.
6. A. S. Richardson 1991 *Electric Power System Research* **21**, 43–55. A study of galloping conductors on a 230kv transmission line.
7. K. F. Jones 1992 *ASCE*, *Journal of Engineering Mechanics* **118**, 92–107. Coupled vertical and horizontal galloping.
8. R. D. Blevins 1990 *Flow-Induced Vibration*. New York: Van Nostrand Reinhold Co. Second edition.
9. Y. M. Desai 1991 *Ph.D. thesis*, *University of Manitoba*. Modelling of planar transmission line galloping.
10. Y. Nakamura 1980 *Journal of Sound and Vibration* **73**, 363–377. Galloping of bundled power line conductors.
11. W. Jianwei 1996 *Ph.D. thesis*, *Universite De Liege*, *Belgium*. Large vibrations of overhead electrical lines.
12. Manitoba Hydro 1992 *Canadian Electrical Association Report*, *Vols* I & II, *Project No*. 321 *T* 672, *Montreal*, *Canada*. Modelling of conductor galloping.
13. Manitoba Hydro 1995 *Canadian Electrical Association Report*, *Phase* II, *Project No*. 321 *T* 672*A*, *Montreal*, *Canada*. Modelling of conductor galloping.
14. P. Yu, A. H. Shah and N. Popplewell 1992 *Journal of Applied Mechanics*, *Transactions of the ASME* **59**, 140–145. Inertially coupled galloping of iced conductors.
15. P. Yu, Y. M. Desai, A. H. Shah and N. Popplewell 1993 *ASCE*, *Journal of Engineering Mechanics* **119**, 2405–2448. Three-degree-of-freedom model for galloping (Parts I and II).
16. R. W. Clough and J. Penzien 1975 *Dynamics of Structures*. New York: McGraw-Hill.
17. Y. M. Desai, N. Popplewell, A. H. Shah and D. N. Buragohain 1988 *International Journal of Computers and Structures* **29**, 1001–1009. Geometric nonlinear static analysis of cable supported structures.
18. K. G. Mcconnell and C. N. Chang 1986 *Experimental Mechanics* **26**, 324–329. A study of the axial–torsional coupling effect on a sagged transmission line.
19. P. Stumpf 1994 *M.Sc. thesis*, *University of Manitoba*, *Winnipeg*, *Canada*. Determination of aerodynamic forces for iced single and twin-bundled conductors.
20. Y. M. Desai, P. Yu, N. Popplewell and A. H. Shah 1995 *Computers and Structures* **57**, 469–489. Finite element modelling of transmission line galloping.

21. Y. M. DESAI, P. YU, N. POPPLEWELL and A. H. SHAH 1996 *Journal of Sound and Vibration* **191**, 469–489. Perturbation-based finite element analyses of transmission line galloping.
22. A. T. EDWARDS and A. MADEYSKI 1956 *Transactions of the AIEE* **75**, 666–686. Progress report on the investigation of galloping of transmission line conductors.
23. O. NIGOL and O. G. BUCHAN 1981 *Transactions of the IEEE* **PAS-96**, 699–720. Conductor galloping: torsional mechanism—Parts I and II.
24. P. C. M. GORTEMAKER 1984 *Kema Science and Technical Reports* (*Netherlands*) **2**, 27–39. Galloping conductors and evaluation of the effectiveness of inspan dampers.
25. A. S. VELETSOS and G. R. DARBRE 1983 *International Journal of Earthquake Engineering and Structural Dynamics* **11**, 367–401. Dynamic stiffness of parabolic cables.
26. R. K. MATHUR, A. H. SHAH, P. G. S. TRAINOR and N. POPPLEWELL 1987 *IEEE Transactions on PWRD*, *Power Delivery* **2**, 908–916. Dynamics of a guyed transmission tower system.

APPENDIX A: ELEMENTS OF M, K_a AND F

A.1. MASS MATRIX, M

The representative elements, m_{ij} $(i, j = 1, 2, 3)$, of the symmetrical mass matrix, **M**, that appear in equation (14) are

$$m_{11} = \int_0^L \int_{A_T} \rho \, \mathrm{d}A f_v^2 \, \mathrm{d}s + \sum_{k=1}^{p} m_{sk} f_v^2(s_k), \qquad m_{22} = \int_0^L \int_{A_T} \rho \, \mathrm{d}A f_w^2 \, \mathrm{d}s + \sum_{k=1}^{p} m_{sk} f_w^2(s_k), \tag{A1}$$

$$m_{33} = \int_0^L \int_{A_T} \rho(y^2 + z^2) \, \mathrm{d}A f_\theta^2 \, \mathrm{d}s + \sum_{k=1}^{p} I_{sk} f_\theta^2(s_k), \tag{A2}$$

$$m_{13} = -\int_0^L \int_{A_T} \rho z \, \mathrm{d}A f_v f_\theta \, \mathrm{d}s \tag{A3}$$

and

$$m_{23} = \int_0^L \int_{A_T} \rho y \, \mathrm{d}A f_w f_\theta \, \mathrm{d}s. \tag{A4}$$

A.2. STIFFNESS MATRIX, K_a

The representative elements, K_{ij} $(i, j = 1, 2, 3)$, of the symmetrical stiffness matrix, $\mathbf{K_a}$, in equation (13) are

$$\begin{aligned} K_{ij} = {} & \sum_{k=1}^{n} D_{ij} \int_0^L \beta_i \beta_j f_{i,s} f_{j,s} \, \mathrm{d}s - n_2 K_{ice} + n_3 \sum_{k=1}^{n} H_k \int_0^L \frac{\partial s}{\partial x} f_{i,s} f_{j,s} \, \mathrm{d}s \\ & + n_4 \sum_{k=1}^{n} (AE)_k \int_0^L \beta_i f_{i,s} Q_k \, \mathrm{d}s - n_5 \sum_{k=1}^{n} H_k \int_0^L \frac{\partial s}{\partial x} f_{i,s} Q_{2k} \, \mathrm{d}s \\ & + n_6 \sum_{k=1}^{n} H_k \int_0^L \frac{\partial s}{\partial x} f_{i,s} Q_{1k} \, \mathrm{d}s + 2 n_7 B_T \sum_{k=1}^{n} \int_0^L f_{4,s} Q_k \, \mathrm{d}s \\ & + n_7 \left(\sum_{k=1}^{n} H_k \int_0^L \frac{\partial s}{\partial x} f_{i,s}^2 r_k^2 \, \mathrm{d}s + \sum_{k=1}^{n} (AE)_k \int_0^L Q_k^2 \, \mathrm{d}s \right) + K_x (f_u^2(0) + f_u^2(L)), \end{aligned} \tag{A5}$$

where

$$D_{ij} = (AE)_k \quad \text{for all } i \text{ and } j \text{ other than 4},$$

$$D_{ij} = B_T \qquad \text{for } i = 4 \text{ or } j = 4, \quad i \neq j,$$

$$D_{ij} = (GJ)_k \quad \text{for } i = j = 4,$$

$$f_{i,s} = \frac{\partial f_i}{\partial s}, \qquad \beta_1 = \frac{\partial x}{\partial s}, \qquad \langle \beta_2, \beta_3 \rangle = \left\langle \frac{\partial y}{\partial s}, \frac{\partial z}{\partial s} \right\rangle, \qquad \beta_4 = 1 \tag{A6}$$

and

$$Q_k = \beta_3 Q_{1k} - \beta_2 Q_{2k}, \qquad Q_{1k} \sim r_k \cos\theta_{k0} f_{4,s}, \qquad Q_{2k} = r_k \sin\theta_{k0} f_{4,s}. \tag{A7}$$

Moreover,

$$n_2 = \begin{cases} 1, & i = j = 4, \\ 0 & \text{otherwise}, \end{cases} \qquad n_3 = \begin{cases} 1, & i = j = 1, 2, 3, \\ 0 & \text{otherwise}, \end{cases}$$

$$n_4 = \begin{cases} 1, & i \leqslant 3,\ j = 4, \\ 0 & \text{otherwise}, \end{cases} \qquad n_5 = \begin{cases} 1, & i = 2,\ j = 4, \\ 0 & \text{otherwise}, \end{cases}$$

$$n_6 = \begin{cases} 1, & i = 3,\ j = 4, \\ 0 & \text{otherwise}, \end{cases} \qquad n_7 = \begin{cases} 1, & i = j = 4, \\ 0 & \text{otherwise}. \end{cases} \tag{A8}$$

Here, $i,\ j = 1, 2, 3, 4$ represent $i, j = u, v, w, \theta$ for convenience, H is the horizontal component of a conductor's static tension, T, and K_{ice}, which is the stiffness due to the eccentric ice, is [24]

$$K_{ice} = \int_0^L \left(\int_{A_T} \rho y \, \mathrm{d}A \right) g f_\theta^2 \, \mathrm{ds}. \tag{A9}$$

Furthermore, K_x is the stiffness due to the static coupling of the span of interest with its adjacent spans and insulator strings. It is given by [25, 26]

$$K_x = \sum_{i=1}^{n} \left(\frac{12(AE)_i H_i^3}{12LH_i^3 + (AE)_i p_{yi}^2 L_x^3} + \frac{p_{yi} L}{L_i} + \frac{W_i}{2L_i} \right). \tag{A10}$$

L_x is the horizontal distance between adjacent towers, p_{yi} is the total vertical load per unit length of the ith conductor whereas W_i and L_i are the total weight and length of the insulator string, respectively.

A.3. AERODYNAMIC LOAD, F

The elements of the aerodynamic load vector, **F**, used in equation (15) are

$$F_y = \tfrac{1}{2} \rho_{air} U_z^2 \, dC_y, \qquad F_z = \tfrac{1}{2} \rho_{air} U_z^2 \, dC_z, \qquad F_\theta = \tfrac{1}{2} \rho_{air} U_z^2 \, d^2 C_\theta, \tag{A11–A13}$$

where

$$C_y = f_{v\theta}(A_{y1}\alpha' + A_{y2}\alpha'^2 + A_{y3}\alpha'^3), \qquad C_z = A_{z_1}\alpha' + A_{z_2}\alpha'^2 + A_{z_3}\alpha'^3,$$

$$C_\theta = A_{\theta_1}\alpha' + A_{\theta_2}\alpha'^2 + A_{\theta_3}\alpha'^3, \tag{A14}$$

$$f_{v\theta} = \frac{2}{L}\int_0^L f_v f_\theta \, \mathrm{d}s, \tag{A15}$$

$$\alpha' = q_\theta - \frac{d}{2U_z}\dot{q}_\theta - \frac{f_{v\theta}}{U_z}\dot{q}_v = \alpha f_\theta \tag{A16}$$

and

$$A_{ij} = \int_0^L a_{ij} f_\theta^{j+1} \, \mathrm{d}s, \quad i = y, z, \theta, \quad j = 1, 2, 3. \tag{A17}$$

The aerodynamic coefficients, a_{ij}, are obtained by curve-fitting experimental, quasi-steady wind loads in the neighborhood of the initially twisted conductor's profile sustained by the moment arising from the eccentric ice weight [19]. The lift and drag coefficients, C_L and C_D, respectively, are given by

$$C_L = C_y \cos\alpha - C_z \sin\alpha, \qquad C_D = C_y \sin\alpha + C_z \cos\alpha. \tag{A18, A19}$$

APPENDIX B: NOMENCLATURE

A, A_{ice}	cross-sectional area of a conductor that is bare and iced respectively
A_T	total cross-sectional area of all the iced conductors in a bundle
A_y, A_z, A_θ	limit cycle amplitudes in plunge, swingback and torsion, respectively
$\bar{A}_y$, $\bar{A}_z$	non-dimensionalized A_y and A_z, e.g., $\bar{A}_y = A_y/s_a$ where s_a is the static sag at midspan
$\bar{A} = \sqrt{\bar{A}_y^2 + \bar{A}_z^2}$	non-dimensional limit cycle amplitude in the yz plane
B_T	axial-torsional coupling
C_L, C_D, C_θ	aerodynamic lift, drag and moment coefficients, respectively, of a bundle
d	diameter of a bare conductor
E, G	modulus of elasticity and shear modulus of a bare conductor
f	the lowest natural frequency in the vertical direction
g	gravitational constant
H	horizontal tension of a conductor
J	inertial moment of a single bare conductor
L, L_x	total length and horizontal span of a conductor
n, p	number of conductors and spacers respectively
n_p	total number of (finite element) nodes
q_i	$(i = u, v, w, \theta)$ generalized co-ordinates
r_i	distance between the reference curve and the center of the ith conductor's cross-section
s	intrinsic co-ordinate along the reference curve
$T^{(i)}$	transformation matrix from local to global co-ordinates

x, y, z	local co-ordinates
X, Y, Z	global co-ordinates
α	wind's angle of attack at the reference curve
ρ_{air}	density of air
ρ	mass density of the iced bundle conductors' total cross-sectional area